Journal of Solid State Chemistry **149,** 155–166 (2000)
Article ID jssc.1999.8514, available online at http://www.idealibrary.com on IDEAL®

Crystal Structure and Electronic Band Structure of $LaTe_2$

Klaus Stöwe

Institut für Anorganische Chemie und Analytische Chemie und Radiochemie, Universität des Saarlandes, 66041, Saarbrücken, Saarland, Germany

Received July 7, 1999; Accepted September 21, 1999

The observation of superstructure reflections indicating a (2×2×1) supercell of the simple anti-Fe_2As structure type made it necessary to redetermine the crystal structure of $LaTe_2$ by single-crystal analysis. In contrast to former investigations revealing tetragonal or orthorhombic symmetry, our analysis showed that $LaTe_2$ crystallizes monoclinic in space group $P1c1$ with the lattice parameters $a = 919.0(1)$ pm, $b = 910.7(1)$ pm, $c = 907.0(1)$ pm, and $\beta = 90.04(1)^\circ$ ($Z = 8$). Compared to the anti-Fe_2As basis structure, the polyanionic square [4^4] nets are distorted in $LaTe_2$ into herringbone patterns of dimer pairs with interatomic distances of 298.7 and 303.6 pm within the dimers. Electronic band structure calculations with the LMTO-ASA method revealed that by the distortion an indirect band gap of ≈ 0.2 eV between bonding and antibonding dimer Te 5*p* states opens up at the Fermi level. But due to a weak direct La–La interaction a single La 5*d* band is lowered in energy around the Brillouin zone center Γ and thus is responsible for the metallic conductivity of this material. This finding is in agreement with magnetic susceptibility data, revealing after diamagnetic correction a temperature-independent Pauli paramagnetism $\chi_{mol} \approx 1.1 \times 10^{-4}$ emu mol^{-1} at 300 K and recordings of the fundamental optical absorption in the energy range of 0.05–1.33 eV, which gave no indications for a band gap in this range.

INTRODUCTION

From a practical point of view it is not possible to understand measured properties without knowledge of the crystal structure of a compound. From the viewpoint of a theorist it is not possible to compute physical properties of substances without receipt of structural information. So the structure is the interconnecting link between the design of a new compound and its practical application in material sciences. Besides, it is not enough to know an averaged structure, but awareness of the true local structure including superstructure and defects are necessary because in many cases these provide key information about the overall electronic structure. In diffraction experiments superstructure reflections are difficult to detect since their intensities are often extraordinarily weak, their statistics poor, and the intensity data evaluation frequently hampered by twinning effects.

In the past crystal structures of a large number of binary compounds were investigated by X-ray diffraction experiments, and so were the structures of the early lanthanoid ditellurides $LnTe_2$ (Ln = La, Ce, Pr, Nd), which were determined to be of anti-Cu_2Sb or anti-Fe_2As type (1–6). This structure type, which is related to the PbFCl type, can be regarded as built up solely from [4^4] nets with a layer sequence of 4^4(Te), 4^4(Ln), $(4^4)^2$(Te), 4^4(Ln), 4^4(Te), 4^4(Te), etc. By "$(4^4)^2$" we denote polyanionic layers packed twice as dense as the other nets. These regular square Te nets thought to cause a metallic conductivity of the compounds mentioned above. By first principles calculations with the DV–X_α method Kikuchi (7) was able to show that in the case of $LaTe_2$ the Fermi surface is mainly contributed from the Te square sheets and that it has several large parallel branches that satisfy the nesting condition for a CDW transition. On the other side the homologous compounds with Se and S are all distorted, so far that the square nets have decomposed into a system of discrete [Q_2] dumb bells (see, e.g., (8)). As we go to the heavier chalcogen elements, the trend is observed that the ratio between second- and first-nearest neighbor distances is decreasing (9). But even elementary tellurium is a semiconductor with helical chains, and not a metal like polonium with an undistorted simple cubic lattice. So from this point of view we would expect for $LaTe_2$ also a distortion of the square sheets of the anti-Fe_2As type. This distortion may cause superstructure reflections so weak that they have failed to be noticed in the early investigations. A clear hint for this thesis came from the enormous enlarged thermal displacement parameter of the sheet Te ions compared to the other ions in the structure refinement of (4) and the observation of $(2 \times 1 \times 1)$ superstructure reflections by transmission electron microscopy (10). Se we started to reinvestigate the crystal structure of $LaTe_2$ and indeed found weak superstructure reflections, too, but they indicated a $(2 \times 2 \times 1)$ superstructure with monoclinic instead of tetragonal (4) or orthorhombic symmetry (10). Additionally, we performed first principles electronic band structure calculations on the new, distorted

0022-4596/00 $35.00

structure with the purpose of checking whether the distortion would change the physical properties of the compound. Supplementarily, the magnetic and electronic transport properties were investigated to support our theoretical results.

EXPERIMENTAL

Sample Synthesis

Black platelike-shaped single crystals of $LaTe_2$ with peach-colored luster up to an edge length of several millimeters were obtained by chemical vapor transport reactions in silica ampoules, with I_2 as the transporting agent in a temperature gradient from 950 to 850°C starting from the elements La (ingot, 99.9 + %, Kelpin, Leimen, Germany) and Te (pieces, > 99.999%, Fluka, Buchs, Switzerland) as already reported earlier (2). The compound was handled under a dry and oxygen-free atmosphere of purified argon in a glove box because it is moisture- and air-sensitive.

X-Ray Single-Crystal Structure Determination

The data collections were carried out with a *P*4 single-crystal diffractometer (Siemens, Karlsruhe, Germany) and the structure solution and refinement with the computer program SHELX-97 (11). Tables 1–3 give a summary of important measurement and refinement data including the refined parameters and Table 4 gives selected interatomic distances below 400 pm. They refer to a unit cell, which was determined by refinement of the diffraction angles of 98 reflections distributed as uniformly as possible in reciprocal space.

Analytical Characterization and Physical Properties Measurements

For a further characterization of the compound $LaTe_2$ with respect to its composition, atomic emission spectrometry with plasma excitation (ICP-AES, Perkin Elmer) was used. For analysis samples consisting of selected single crystals were sealed in capillaries of 2-mm diameter, subsequently opened in an autoclave with a Teflon inlet, and dissolved in a HNO_3/HCl mixture. Further details are given in (12).

To support the analytical data, the density of samples consisting of several single crystals was measured. This was done by a gas displacement pycnometer of type Accupyc 1330/1cc (Micromeritics) with helium as the working gas. To measure the density of the air- and moisture-sensitive samples, the complete pycnometer was placed in a glove box under a dried and oxygen-free argon atmosphere.

Magnetic data were recorded with samples synthesized by chemical vapor transport reactions and enclosed in a gelatin capsule, which is again sealed in Suprasil glass capillary of 200-mm length and a reduction in the middle of the capillary to hold the gelatin capsule. Susceptibility measurements were performed with an MPMS SQUID magnetometer (Quantum Design) as a function of magnetic field strength from 320 K down to 5 K. Diamagnetic corrections were applied with the increments $\chi_{mol}(La^{3+}) = -2 \times 10^{-5}$ emu mol^{-1} and $\chi_{mol}(Te^{2-}) = -7 \times 10^{-5}$ emu mol^{-1} (13).

To get information about the electronic transport properties the fundamental absorption (DRIFT) of powered specimens in the frequency range of 10800–380 cm^{-1} was measured a FT-IR System 2000 spectrometer (Perkin Elmer Co.) and the diffuse reflection accessory "The Selector" (Graseby Specac) at ambient temperature in a specially designed sample cell, in which the sample is protected from

TABLE 1
Measurement and Refinement Data for $LaTe_2$ in the X-Ray Single-Crystal Structure Analysis

Measurement temperature	293 K
Lattice parameters	
a	919.0(1) pm
b	910.7(1) pm
c	907.0(1) pm
β	90.04(1)°
No. of formula units per cell	8
Calculated density	6.896 g cm^{-3}
Measured density	6.85(1) g cm^{-3}
Space group	*P*1*c*1
Measured range of reciprocal space (Mo $K\alpha$)	$3 < 2\theta < 60°$ (all octants)
Type of data collection/scan width	ω/0.9° in 96 steps
No. of observed reflections	8853
No. of nonequivalent reflections	4445
Absorption correction	Numerical[a,b]
Crystal color	Lustrous black
Crystal size	$0.08 \times 0.15 \times 0.32$ mm^3
Linear absorption coefficient	261.7 cm^{-1}
Internal *R* value[c]	5.16%
Structure solution	Transformed anti-Fe_2As model
Structure refinement	Full-matrix least-squares
Program for structure solution and refinement	SHELX-97[d]
Extinction parameter empirical with $F^* = F[1 + 0.002\chi F^2/\sin(2\theta)]^{-1/4}$	0.00187(1)
No. of independent parameters	113
R values ($w = 1/\sigma(F_0)^2$)	$wR_2 = 0.0585$

[a] Herrendorf, W., "HABITUS, Program for the Optimization of the Crystal Description for a Numerical Absorption Correction on the Basis of Appropriate Psi-Scanned Reflections," Karlsruhe, Germany 1992.

[b] Alcock, N. W., Marks, P. J., and Adams, K.-G., "ABSPSI, Absorption Correction and Refinement of the Crystal Habitus," Karlsruhe, Germany 1994.

[c] Adams, K.-G., "MITTELN, Averaging Symmetry-Equivalent Reflections," Karlsruhe, Germany 1995.

[d] Sheldrick, G. M., "SHELX-97, FORTRAN-77 Program for the Refinement of Crystal Structures from Diffraction Data," Göttingen, 1997; Sheldrick, G. M., *Acta Cryst. A* **46,** 467 (1990).

TABLE 2
Positional Parameters and Equivalent Isotropic Displacement Factors (pm^2) of $LaTe_2$

Atom	Wyck	x	y	z	U_{eq}
La(1)	2a	0.7263(1)	− 0.0038(1)	0.0059(1)	140.8(2)
La(2)	2a	0.7270(1)	0.4962(1)	− 0.0103(1)	155.3(2)
La(3)	2a	0.2749(2)	0.2498(2)	0.2474(3)	166.8(3)
La(4)	2a	0.2748(2)	0.2504(2)	0.7475(3)	164.6(3)
Te(11)	2a	0.0006(1)	0.2421(1)	− 0.0009(2)	235.4(3)
Te(12)	2a	− 0.0006(2)	0.7380(1)	0.0016(2)	220.3(3)
Te(13)	2a	0.0003(1)	− 0.0020(2)	0.2669(1)	116.6(2)
Te(14)	2a	− 0.0010(1)	0.4994(2)	0.2277(1)	164.4(2)
Te(21)	2a	0.3660(1)	− 0.0009(1)	0.0009(1)	144.7(2)
Te(22)	2a	0.3657(1)	0.4991(1)	− 0.0047(1)	141.3(2)
Te(23)	2a	0.6324(1)	0.2503(2)	0.2469(2)	133.4(2)
Te(24)	2a	0.6327(2)	0.2504(2)	0.7468(3)	133.3(3)

Note. Equivalent isotropic U calculated by $\frac{1}{3}[U_{22} + (U_{11} + U_{33} + 2U_{13}\cos\beta)/\sin^2\beta]$.

moisture and oxygen by a KBr window and a Viton seal. As reference, KBr dried at 400°C under high vacuum conditions was used.

CRYSTAL STRUCTURE

X-ray diffraction experiments on single-crystals of $LaTe_2$ revealed weak superstructure reflections, which indicated a $(2 \times 2 \times 1)$ supercell of the simple anti-Fe_2As structure type. $LaTe_2$ crystallizes monoclinic with a pseudo-orthorhombic unit cell in contrast to former investigations, which found a tetragonal (4) or orthorhombic space group (10). To find a structure model for refinement, from extinction conditions the orthorhombic space groups *Pbam* and *Pba*2 could be deduced at the early stages of refinement with $a = 907.0(1)$, $b = 910.7(1)$ and $c = 919.0(1)$ pm. But as group–subgroup relations have shown in (Fig. 1), *Pbam* is not a subgroup of space group $P4/nmm$ of the anti-Fe_2As type. So a structure model in space group *Pba*2 was tried in the beginning of the refinement. But difference electron density synthesis maxima and averaging of symmetry-equivalent reflections clearly indicated a reduced Patterson symmetry of $P12/m1$ instead of $P2/m2/m2/m$. Because of this finding, in the subsequent refinements the subgroup $P1a1$ or, in a standard setting, space group $P1c1$ was used with the lattice parameters $a = 919.0(1)$, $b = 910.7(1)$ and $c = 907.0(1)$ pm, and $\beta = 90.04(1)°$. To get starting values for positional parameters in the refinement cycles, we transformed the original ones determined by (4) in space group $P4/nmm$ according to the symmetry tree already given in Fig. 1. Appreciable changes in positional parameters during refinement were observed only for the Te ions within the square nets (Te(1n), $n = 1$–4 in Table 2), whereas the other Te anions (Te(2n), $n = 1$–4) and the La cations (La(n), $n = 1$–4) remain almost at their positions as in the anti-Fe_2As structure type. A significant decrease in wR_2 was achieved not only by reduction of symmetry from orthorhombic to monoclinic but also by the refinement of a

TABLE 3
Anisotropic Displacement Factors (pm^2) of $LaTe_2$

Atom	U_{11}	U_{22}	U_{33}	U_{23}	U_{13}	U_{12}
La(1)	101(3)	177(3)	145(4)	30(5)	− 48(3)	− 2(4)
La(2)	115(4)	172(3)	179(5)	− 22(7)	− 49(3)	7(4)
La(3)	157(6)	156(4)	187(5)	− 5(2)	− 70(8)	− 30(6)
La(4)	149(6)	156(4)	189(5)	4(2)	− 71(8)	14(6)
Te(11)	135(4)	245(4)	327(6)	89(3)	− 88(9)	5(6)
Te(12)	112(5)	244(4)	305(7)	17(4)	− 86(9)	27(6)
Tel(13)	84(3)	159(3)	107(3)	8(4)	− 32(4)	− 16(9)
Te(14)	120(4)	162(3)	211(4)	− 53(4)	− 11(6)	− 22(9)
Te(21)	146(4)	147(3)	141(5)	1(7)	− 46(3)	2(4)
Te(22)	146(4)	131(3)	147(5)	0(8)	− 44(3)	− 0(4)
Te(23)	77(5)	164(4)	159(4)	− 5(2)	− 43(9)	− 2(6)
Te(24)	88(6)	160(4)	152(5)	− 8(2)	− 40(9)	14(6)

Note. The dimensions are in accordance with the following formula: $-2\pi^2 \sum_i \sum_j U_{ij} h_i h_j a_i^* a_j^*$.

TABLE 4
Selected Interatomic Distances below 400 pm in $LaTe_2$ (pm)

	La–Te Distances		
La(1)–Te(24)	324.9(2)	La(2)–Te(24)	325.8(2)
La(1)–Te(23)	329.8(2)	La(2)–Te(14)	330.2(2)
La(1)–Te(21)	331.1(1)	La(2)–Te(23)	330.8(2)
La(1)–Te(13)	332.5(1)	La(2)–Te(22)	332.1(2)
La(1)–Te(23)	336.2(2)	La(2)–Te(12)	333.6(2)
La(1)–Te(11)	337.3(1)	La(2)–Te(23)	334.9(2)
La(1)–Te(24)	340.9(2)	La(2)–Te(24)	339.4(2)
La(1)–Te(12)	343.9(2)	La(2)–Te(11)	341.8(2)
La(1)–Te(13)	345.5(1)	La(2)–Te(14)	345.1(2)
La(3)–Te(23)	328.5(2)	La(4)–Te(24)	328.9(2)
La(3)–Te(22)	331.4(2)	La(4)–Te(22)	329.7(2)
La(3)–Te(21)	331.4(2)	La(4)–Te(21)	330.8(2)
La(3)–Te(21)	332.4(2)	La(4)–Te(22)	333.8(2)
La(3)–Te(22)	332.9(2)	La(4)–Te(21)	333.9(2)
La(3)–Te(11)	338.0(2)	La(4)–Te(12)	337.4(3)
La(3)–Te(14)	341.0(2)	La(4)–Te(13)	339.3(2)
La(3)–Te(13)	341.4(2)	La(4)–Te(11)	340.2(2)
La(3)–Te(12)	342.8(2)	La(4)–Te(14)	341.3(2)
	Te–Te Distances		
Te(11)–Te(13)	303.6(2)	Te(12)–Te(14)	298.7(2)
Te(11)–Te(14)	313.0(2)	Te(12)–Te(13)	321.2(2)
Te(11)–Te(13)	329.2(2)	Te(12)–Te(14)	329.4(2)
Te(11)–Te(14)	340.6(2)	Te(12)–Te(13)	337.6(2)
Te(13)–Te(11)	303.6(2)	Te(14)–Te(12)	298.8(2)
Te(13)–Te(12)	321.2(2)	Te(14)–Te(11)	313.0(2)
Te(13)–Te(11)	329.2(2)	Te(14)–Te(12)	329.4(2)
Te(13)–Te(12)	337.6(2)	Te(14)–Te(11)	340.6(2)

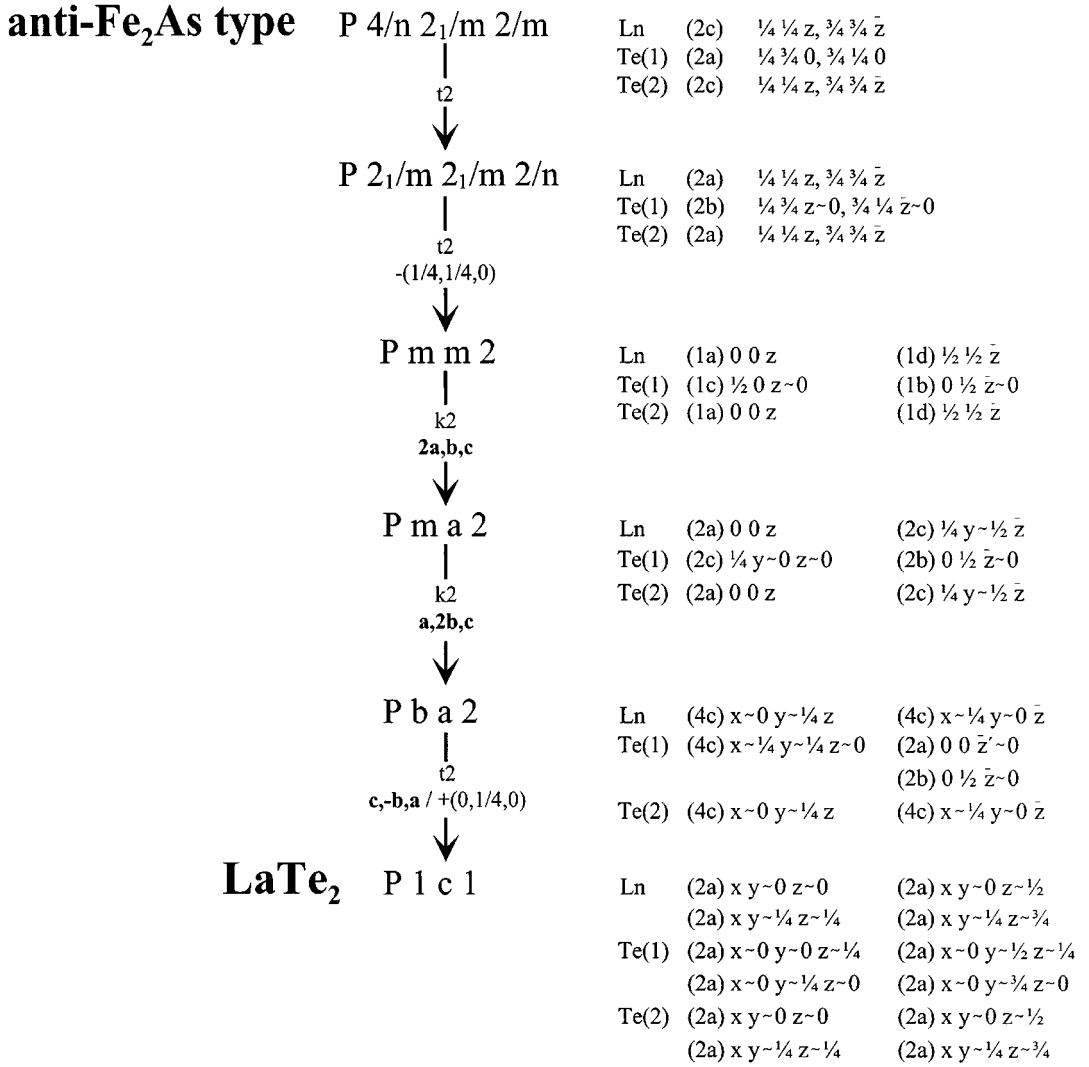

FIG. 1. Symmetry relations between the space group of the anti-Fe_2As structure type $P4/nmm$ and the actual space group of $LaTe_2$ $P1c1$.

"Vierling" (German for twin with four components) with the twin law of an m_x mirror plane and additionally racemic twinning with the twin refinement method of Pratt, Coyle, and Ibers (14) and Jameson, Schneider, Dubler, and Oswald (15) as implemented in the program SHELXL (11). With a numerical absorption correction the wR_2 finally converged to 0.0585 with the twin components $twc_1 = 0.042(5)$, $twc_2 = 0.45(6)$, $twc_3 = 0.398(6)$, and $twc_4 = 1 - twc_1 - twc_2$ twc_3. Twinning by a diagonal mirror plane of a $(2 \times 1 \times 1)$ superstructure as in "form A" of the monoclinic compound $LaSe_2$ (8), which would also give an apparent unit cell as observed, could be ruled out because reflections with indices (hhl) and h odd had distinct intensities.

The difference of the actual structure model to former investigations is lying entirely in the topology of the square $[4^4]$ net. Like a CDW the Te($1n$) (n = 1–4) located in the square nets have distorted into layers of $[Te_2]$ dimers, which are arranged in a double-herringbone pattern as depicted in Fig 2. Topologically, the only difference to the compound $LaSe_2$ is that in $LaTe_2$ the dimers are forming pairs, whereas in $LaSe_2$ isolated dimers are arranged in a herringbone pattern (Fig. 3, upper part). As expected for tellurides, the differentiation between the polyanionic interatomic distances within the distorted tellurium sheet is much less distinct than those in the other polychalcogenides like, e.g., $LaSe_2$ (see Introduction). In $LaTe_2$ they are all lying in the range 298.7–340.6 pm. Within the dimers the telluriums are 298.7 and 303.6 pm apart (see Table 4). The largest interatomic distances within a single sheet are observed from one dimer to the neighboring one of the dimer pair (337.6 and 340.6 pm). To give a feeling for the differentiation, the ratio between longest and shortest

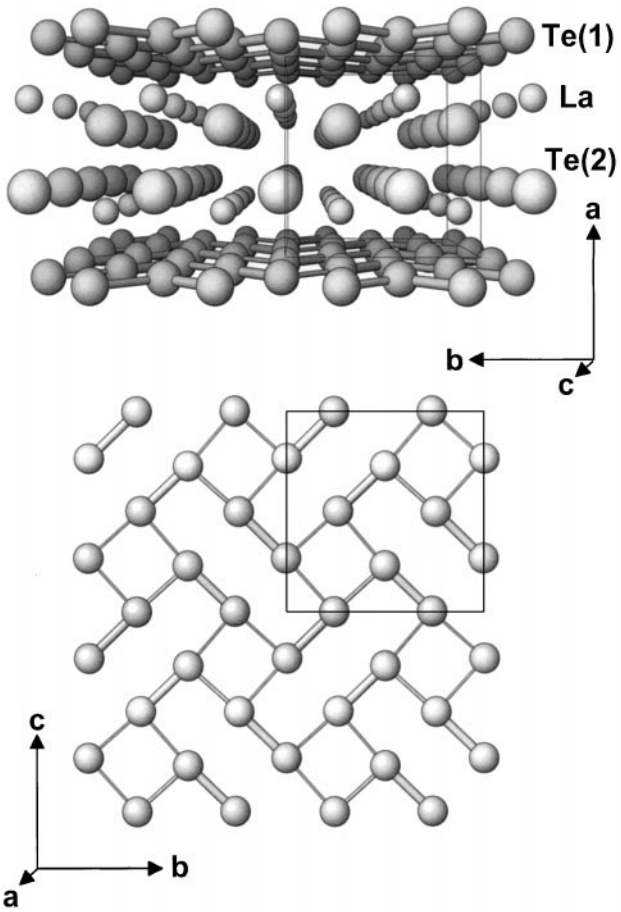

FIG. 2. Crystal structure of $LaTe_2$ in two different projections. Top: [001] projection. Bottom: single distorted square sheet in [100] projection. The various interatomic distances are indicated by different stick thicknesses: 290–301 pm in bold outline, 310–320 pm in medium thickness, and 320–330 pm in fine thickness.

interatomic distances within a single layer may be calculated. It is 1.39 for $LaSe_2$ and only 1.14 for $LaTe_2$. A value very similar to the former ratio of 1.43 is found for the selenium compound $La_{10}Se_{19}$, whose structure is a ordered-defect variant of the anti-Fe_2As type (16). Instead of regular square nets we find in the layers of $La_{10}Se_{19}$ isolated Se^{2-} anions, vacancies, and Se_2^{2-} dimers in the ratio 1:1:4 (Fig. 3, lower part).

The existence of additional compounds with a composition very close to a 1:2 ratio of metal to chalcogen opens the question of the stoichiometric composition of the investigated crystals, although there were no hints for nonstoichiometry from the refinement procedure. The analysis by ICP-AES of selected single crystals of the product synthesized by chemical vapor transport reactions revealed a composition of $LaSe_{1.99(5)}$ and thus gave no hints on a nonstoichiometric composition. This result is also confirmed by pycnometric density measurements, which yielded a measured density of $\rho_m = 6.85(1)$ gcm^{-3} compared to a calculated density of $\rho_x = 6.896$ gcm^{-3}.

DETAILS OF THE ELECTRONIC BAND STRUCTURE CALCULATIONS

LDA LMTO-ASA Calculations

The self-consistent *ab initio* band structure calculations of $LaTe_2$ have been performed by the use of density functional theory in the local density approximation (LDA) with the

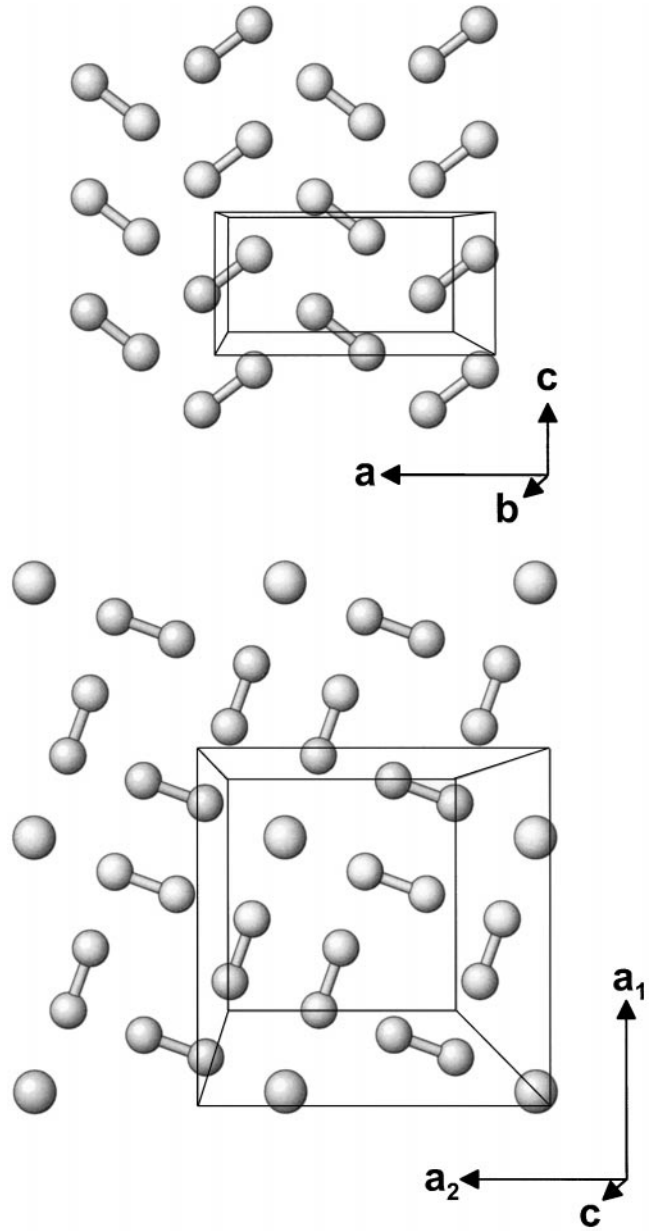

FIG. 3. Distortion pattern for the selenium sheets in $LaSe_2$ in the form of a herringbone pattern (top) and $La_{10}Se_{19}$ with isolated Se^{2-} anions, vacancies, and Se_2^{2-} dimers in the ratio 1:1:4 (bottom).

TABLE 5
Muffin Tin Sphere Radii (in pm) Used in the LMTO-ASA Calculations

La(1)	La(2)	La(3)	La(4)	Te(11)	Te(12)	Te(13)
195.5	196.3	197.5	197.9	175.8	173.2	175.3
Te(14)	Te(21)	Te(22)	Te(23)	Te(24)	E	E1
173.2	180.3	179.3	179.3	177.5	123.8	123.6
E2	E3	E4	E5	E6	E7	E8
123.8	124.0	113.2	111.8	111.7	109.9	73.9
E9	E10	E11	E12	E13	E14	
73.6	74.7	73.4	71.3	74.9	72.6	

LMTO-47 package of Andersen *et al.* (17). The calculation within the atomic spheres approximation (ASA) includes corrections for the neglect of the interstitial region and the partial waves of higher order (ASA + combined correction). To reduce as much as possible the overlap between the atomic spheres, empty interstitial spheres were added to the potential. The construction of the ASA radii was done by an automatical procedure of the program package using the method proposed by Andersen (18). In detail, the sphere radii were given in Table 5. The basis set consisted of the La 6*s*, 5*d*, and 4*f* LMTOs, the Te 5*s* and 5*p* LMTOs, and the interestitial 1*s* LMTOs. The La 6*p*, the Te 5*d* and 4*f*, and the interstitial *p* and *d* partial waves were included only in the tails of these LMTOs according to the Löwdin down folding procedure (18). The *k*-space integration was performed by the tetrahedron method. Charge self-consistency and properties calculations were obtained from 4400 irreducible *k* points. As measure for the bonding strengths we computed the COHP function (crystal orbital Hamiltonian population) which is the Hamiltonian population weighted density of states. As recommended (19), a reduced basis set in which all empty sphere LMTOs have been downfolded was used for the COHP calculation.

For the purpose of comparison with literature data we also performed extended-Hückel calculations using the program EHMACC (20).

Brillouin Zone

The reciprocal lattice vectors of $LaTe_2$ together with the first Brillouin zone are shown in Fig. 4. High-symmetry points were labeled following Miller and Love (21).

RESULTS OF THE LMTO-ASA ENERGY BAND CALCULATIONS

Starting with undistorted square nets of tellurium as in the anti-Fe_2As structure type, we would expect $LaTe_2$ to be metallic, as was shown by former calculations (7, 10). By dimers being formed, at a glance the conductivity of the compound should change from metallic to semiconducting, as one would expect for a Peierls transition. But there might be reasons why the metallic conductivity persists, even in the distorted case. An example is given by the compound TlTe, which shows an anionic analogue to a Peierls transition at 172 K attended by a resistivity hump of the factor 2–3 (22). TlTe reveals linear Te chains, which change from equidistant to alternating during transition. Since not all chains are affected by the transition, the compound keeps its metallic behavior, even below the transition temperature of 172 K. But even in the case that the structural elements causing metallic conductivity are completely involved in the distortion, there might be further reasons for a persisting metallic conductivity, as in the compound $ZrTe_3$ (23). Beyond the trichalcogenides of $ZrSe_3$ structure type, $ZrTe_3$ is the only compound which has metallic properties despite distinct chain alternation. This is because the dimensionality of the conductivity in $ZrTe_3$ is beyond that of the one-dimensional chain. According to these findings, we subdivided the following discussion for $LaTe_2$ into two parts. In the first part we will make evident the changes that occur on the distortion of the Te square nets into a system of discrete dimers in the form of a double-herringbone pattern. In the second part we modify our approach of considering only isolated Te sheets and focus our attention at further interactions, which possibly may alter the electronic structure and, therefore, the conductivity properties of the compound.

The calculated energy band structure of $LaTe_2$ is shown in Fig. 5 for the wave vector **k** along the following lines (see Fig. 4): $\Gamma = (0,0\,0)$ to $Z = (0,0,\frac{1}{2})$ to $C = (0,\frac{1}{2},\frac{1}{2})$ to $Y = (0,\frac{1}{2},0)$ and then back to $\Gamma = (0,0,0)$, and furtheron to $B = (\frac{1}{2},0,0)$ to $D = (\frac{1}{2},\frac{1}{2},0)$ and finally back to $Y = (0,\frac{1}{2},0)$. The coordinates are given in units of the reciprocal lattice vectors. The band structure was projected onto orthogonal LMTOs normalized to unity within the ASA spheres. To simplify matters, we differentiate in the following only three

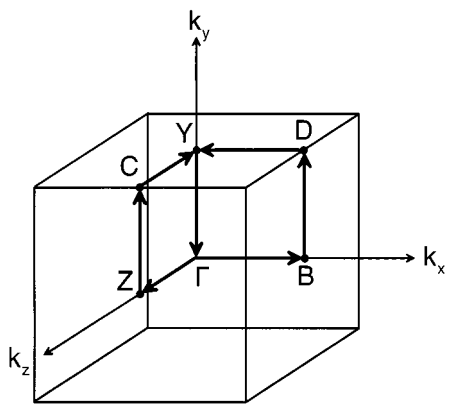

FIG. 4. Brillouin zone of $LaTe_2$ and high symmetry points.

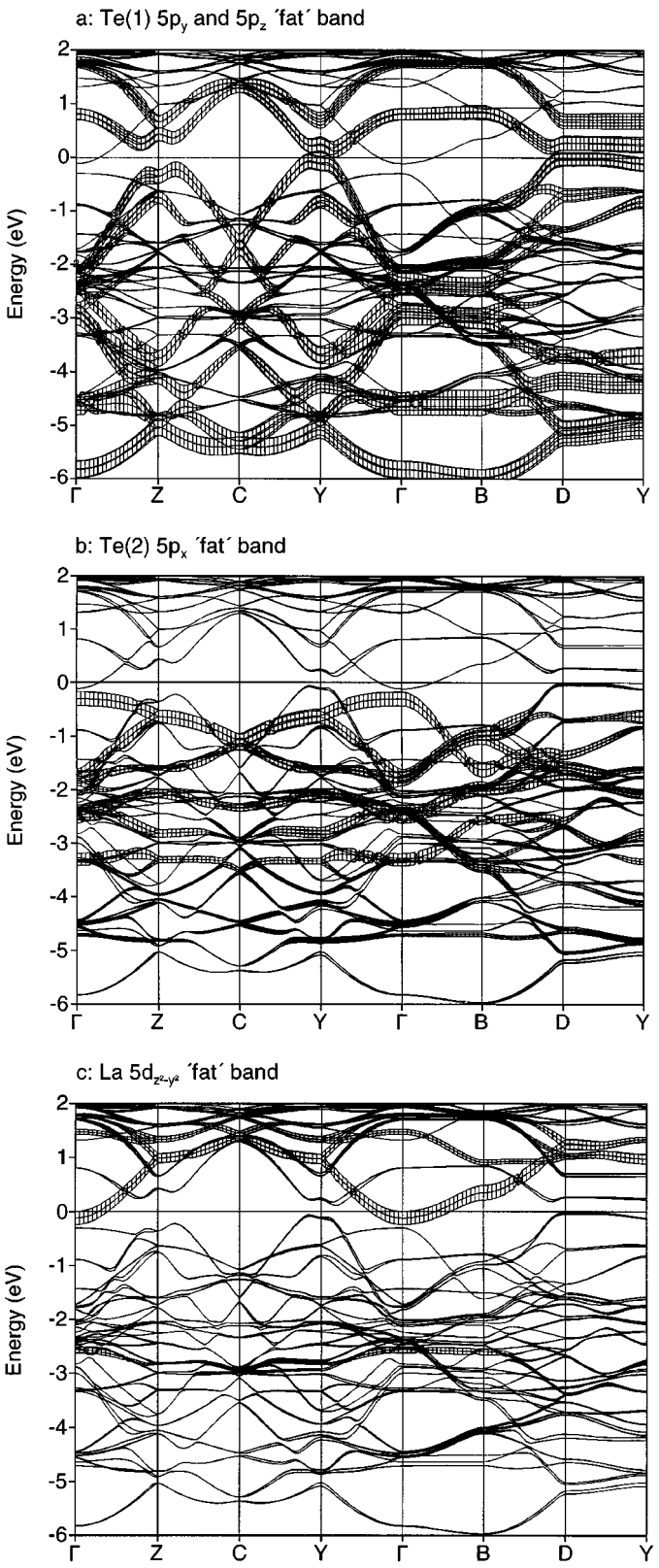

FIG. 5. Energy bands of $LaTe_2$ decorated with orthonormal-orbital characters. A pure band state is given the energy width 0.4 eV: (a) Tel(1) $5p_y$ and $5p_z$ fat band; (b) Te(2) $5p_x$ fat band; (c) La $5d_{z^2-y^2}$ fat band.

types of ions, La, Te(1), and Te(2) since the chemical environments of the different ions of each type are quite similar. For the sake of representation, we set the Fermi energy $E_F = 0$ eV in this figure and throughout this paper.

In Fig. 5a the dispersion relation of energy bands decorated with Te(1) $5p_y$ and $5p_z$ orbital character is shown in a "fat" band representation. According to the transformation of the unit cell axes into a standard setting (space group $P1c1$), the crystallographic bc plane is now the plane in which the distorted square nets are running. The LMTO band structure reveals in the energy range of -6 to 2 eV contributions mainly from Te p bands. Direct at the Fermi level we find Te(1) $5p_y$ and $5p_z$ states with an indirect gap of approximately 0.2 eV separating occupied from unoccupied states. Along the line D to Y the Te(1) p_y and p_z bands are running almost horizontally, causing a van Hove singularity with a pronounced density of states just a few meV below E_F. So without further interactions the compound $LaTe_2$ should be a small band gap semiconductor. Above the Fermi level all in all four unoccupied $5p$ bands are found because there are just four dimers within each unit cell. This is depicted schematically in Fig. 6, which shows our attempts to reproduce the dispersion relation of the Te(1) bands in the LMTO band structure by an isolated sheet cut out from the $LaTe_2$ crystal structure with the much less sophisticated, but nevertheless instructive, EH method. At the right side an orbital analysis of these four unoccupied bands is given at the zone center Γ, revealing that they have a high degree of antibonding character. With four unoccupied bands in each unit of four dimers, a formal 8-fold negative charge is to be assigned, resulting in a purely ionic formulation of the compound $LaTe_2$ as $La^{3+}Te(1)^{-}Te(2)^{2-}$. Thus, $LaTe_2$ would behave completely analogous to the sulfur and selenium compounds, with the only difference of forming double- instead of simple-herringbone patterns. But as we will see later, there are also distinct differences between the compounds mentioned above.

The question arises as to what the energetic differences between the two observed patterns are. To answer this question for the simple herringbone pattern, Lee and Foran (9) combined a computational method, which models the energies in the $LaSe_2$ system as a sum of an ionic energy term caused by the ionic constituents of the lattice and a covalent-metallic energy term as the result of the Se–Se interaction, with a method of steepest descent to locate the local energy minima for the $LaSe_2$ stoichiometry. Beyond different considered supercell alternatives for the $LaSe_2$ stoichiometry, the calculated energy was lowest for the observed herringbone pattern of the $(2 \times 1 \times 1)$ superstructure. Lee and Foran (9) found that this energetic stability can be understood by considering HOMO (highest occupied molecular orbital) to LUMO (lowest unoccupied molecular orbital) interactions of the Se_2^{2-} dimers and concluded that these interactions will be strongest when

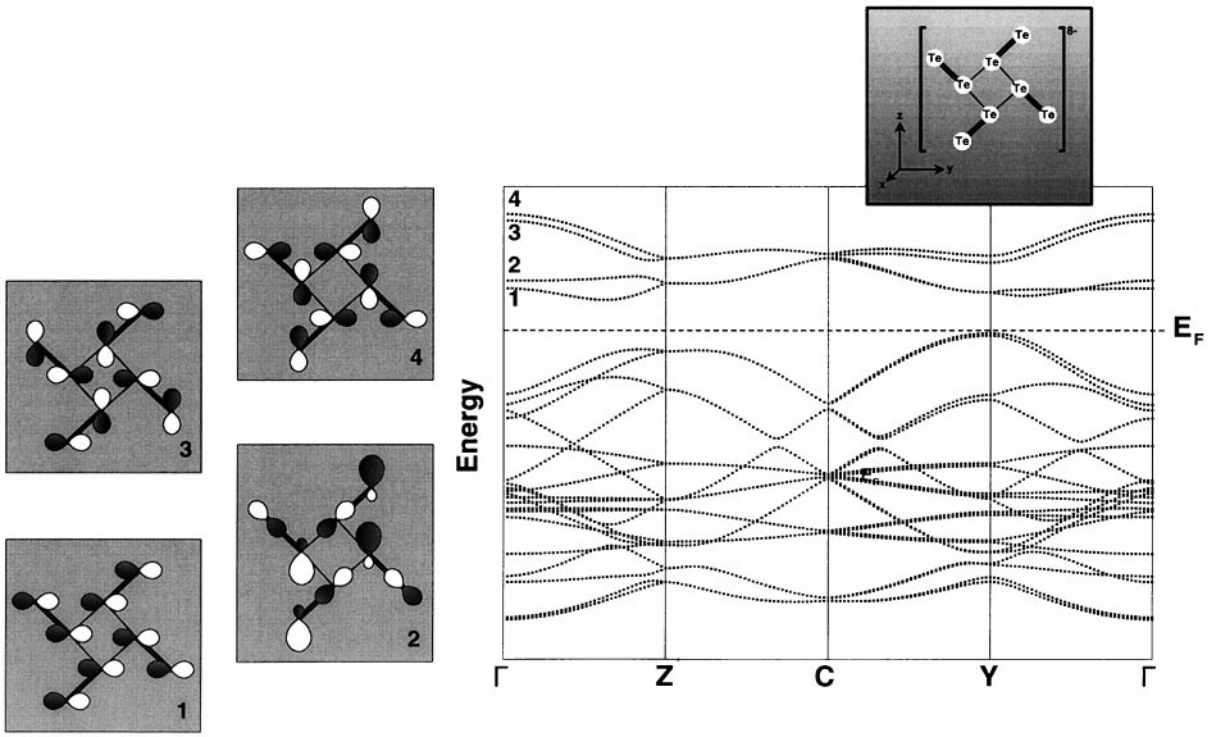

FIG. 6. Results of the attempts to model the Te1(1) p band dispersion of the calculated LMTO band structure by the EH method. As Hückel parameters for Te, $H_{ii}(5s) = -20.8$ eV, $\xi(5s) = 2.51$ and $H_{ii}(5p) = -11.8$ eV, $\xi(5p) = 2.16$ were used.

neighboring Se_2^{2-} dimers (d(Se–Se) = 245 pm) are perpendicular to one another (Fig. 7). On the other hand, 0° or 180° interactions are much less favorable. The energetic preference of 90° interactions is reflected in the interatomic distances to the second-nearest neighbors: neighbors in a 90° arrangement are in in $LaSe_2$ 313 pm apart, in an 180° arrangement 340 pm. Although their calculations did not include the alternative of a double-herringbone pattern found in $LaTe_2$, from the point of view of the HOMO–LUMO interactions, the double- and the simple-herringbone pattern should have a very similar energetic stability. This is due to the fact that both arrangements have the same number of two 90° and one 0°/180° interactions per selenium or tellurium. To explain that in the tellurium compound the double-herringbone pattern is preferred, we have to consider also all the second-nearest neighbor interactions. These are all interatomic distances within a sheet below the ionic radii sum of Te^{2-}, i.e., below the maximum of 340.6 pm (see above). These secondary interactions are almost absent in the analogous selenide, where we have a pronounced differentiation between first- and second-nearest neighbors. To get further insight in the secondary interactions in $LaTe_2$, we calculated the crystal orbital Hamiltonian population COHP function, which gives results similar to those of the well-known COOP. The results of our calculations are presented in Fig. 8 together with the corresponding integrated COHP curves. ICOHP values at the Fermi level are also given. We note that the two symmetry-independent Te(1)–Te(1) interactions within the dimers are the strongest within a single sheet with integrated COHP values of 0.97 and 0.93 eV for d(Te(12)–Te(14)) = 298.7 pm and d(Te(11)–Te(13)) = 303.6 pm, respectively. They allow us to gauge the strengths of the other Te interactions relative to these. Correspondingly, the calculations made it evident that beyond the different homonuclear interactions only those with $d < 320$ pm are of considerable interest. Above 320 pm antibonding contributions at E_F have lowered the integrated COHP to values below one-third of the ones of the dimers. These facts are leading us to a new description of the Te(1) sheets based on bonding

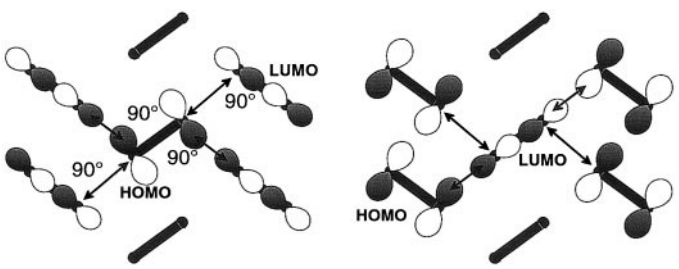

FIG. 7. HOMO–LUMO interactions at 90° in $LaSe_2$.

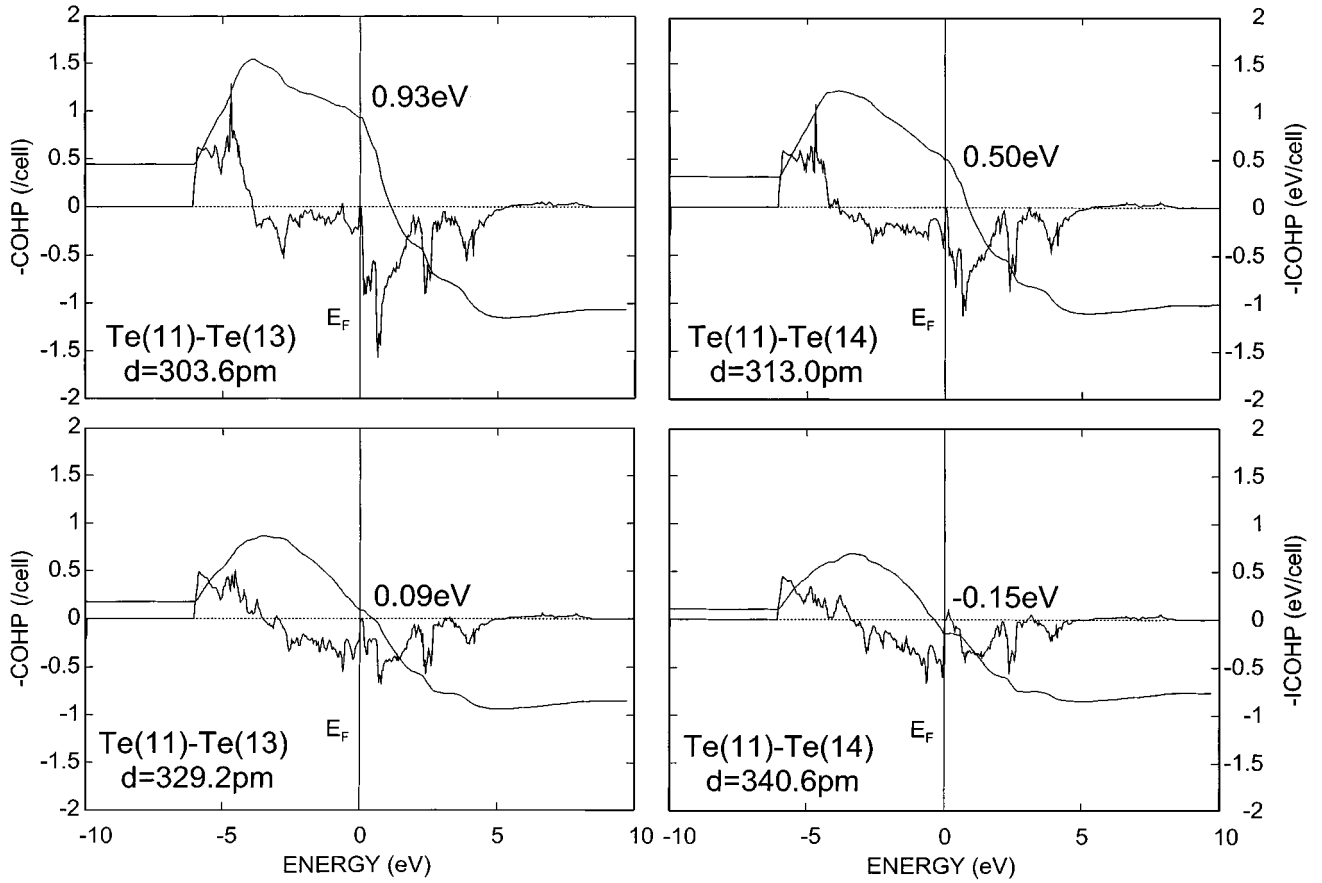

FIG. 8. Crystal orbital Hamiltonian population, COHP, exemplarily for the Te(11)–Te(1*n*) ($n = 3, 4$) interactions in $LaTe_2$. The integrated COHP values up to the Fermi level are given.

considerations. The COHP function suggests that we have to regard the Te(1) sheet as a simple-herringbone arrangement of L-shaped [Te_4] units, interconnected by weak interactions to zig–zag chains, which are depicted in Fig. 9. On the other hand, analogous secondary interactions within sheets of $LaSe_2$ topology would result in a simple primitive arrangement of L-shaped units. Transferring the concept of HOMO–LUMO interactions of Lee and Foran (9) faithfully onto these L-shaped [Te_4] units, we have to conclude that again the herringbone motif with optimized covalent and ionic forces should be the most favorable structural alternative compared to the simple primitive arrangement.

Now that we have established a detailed bonding description for an isolated Te(1) sheet, it remains for us to focus our attention on further interactions, which may alter our present model of the electronic structure of $LaTe_2$. We consider now the remaining structural elements, i.e., the slabs built up from La and Te(2). Fat band representations of the Te(2) $5p_x$ and the La $5d_{z^2-y^2}$ character are given in Figs. 5b and 5c, respectively. From Fig. 5c we can gather that around point Γ one single La 5*d* band comes down in energy below the top edge of the occupied Te(1) 5*p* bands. This single La 5*d* band was identified as mainly of $5d_{x^2-y^2}$ character or, after rotation by 90° about the *y* axis, of $5d_{z^2-y^2}$ character, respectively. The dispersion of this band is quite pronounced with an energy increase both in the direction of the layers, i.e., the special points *Z* and *Y*, and also in the direction of point *B*, indicating a reasonable interaction. As the shortest observed interatomic La–La distances are relatively large ($d = 453.3$–455.6 pm) compared to distances in the corresponding metal (d(La–La) = 375 pm (24)) or typical d^1-configurated metallic compounds, as e.g. LaI_2 (d(La–La) = 392 pm (25)), the question arises as to what the nature of the energetic lowering of the single La 5*d* band is. At point Γ a few hundred meV below the La-centered band another energetically high-lying band is observed, which is mainly of Te(2) $5p_x$ character (see Fig. 5b) with small contributions from Te(1) $5p_x$ orbitals. In contrast to the energetically higher lying band, the energy of this band decreases in the directions of reciprocal space given above. An analysis of

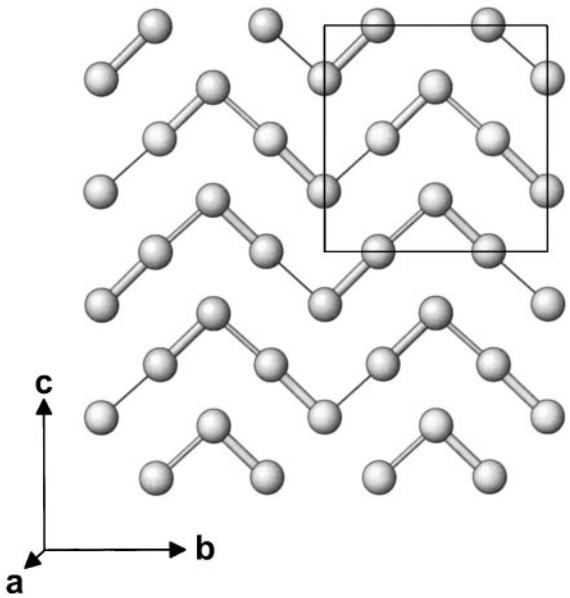

FIG. 9. Single distorted Te(1) square sheet of $LaTe_2$ taking into account secondary Te–Te interactions. These result in a description of these sheets as L-shaped [Te_4] units interconnected by weak interactions to zig–zag chains in the [010] direction.

the atomic orbitals for these two selected crystal orbitals at point Γ is depicted schematically in Fig. 10. Both crystal orbitals represent the complete in-phase combination of La $5d_{z^2-y^2}$ and Te(2) $5p_x$ orbitals, respectively. For La $5d_{z^2-y^2}$ orbitals this situation is energetically highly favorable, but for the Te(2) $5p_x$ orbitals highly unfavorable. It is also the consequence of a very strong covalent La–Te interaction, which can again be taken from the calculations of the COHP function in Fig. 11. Beyond the different La–Te interactions the strengths of the La–Te(2) bonds with integrated COHP values of 0.98–1.28 eV are significantly larger than those of La–Te(1) bonds with ICOHP = 0.69–0.86 eV. For all of the nine neighbors the maximum of the integrated COHP is found near the Fermi level, indicating occupation of almost the maximal possible number of bonding states (Fig. 11, left part). In contrast to this maximal La–La interaction (Fig. 11, right side) is found not before 2 eV above Fermi level and reveals at E_F only a small plateau in the integrated COHP at a value of 0.26 eV. Due to these additional homonuclear La interactions the compound $LaTe_2$ should have a metallic or even semimetallic conductivity characteristic. The corresponding Fermi surface is quite simple, revealing small elliptical electron pockets with semiaxes extensions of about 0.14 and 0.20 in units of the reciprocal lattice vectors and a number of 61[1] occupied bands around special points Γ.

To examine the conductivity characteristic of $LaTe_2$, we performed magnetic susceptibility and optical band gap measurements. In the temperature range from 5 to 330 K the magnetic susceptibility is nearly field- and temperature-independent, revealing negative values. At very low temperatures below 10 K a paramagnetic impurity of a concentration $< 0.1\%$ (referring to Gd as impurity) is resulting in a small increase of susceptibility data (see Fig. 12). After taking a molar diamagnetic offset into account, a temperature-independent Pauli paramagnetism with an averaged value of $\chi_{mol} = +1.1 \times 10^{-4}$ emu mol^{-1} at 300 K was observed. This value is in the same order of magnitude as that for the d^1-configurated metallic compound LaI_2 ($\chi_{mol} = +1.0 \times 10^{-4}$ emu mol^{-1} at 300 K (26)). In the case of $LaTe_2$ the high density of states at the Fermi level is due not only to the (relative low) number of La $5d$ states but also to a certain number of Te(1) $5p$ states, which can be seen in our charge density calculations as Te(1) $5p_y$ and $5p_z$ bands running almost horizontally from special points D to Y with the Fermi level touching these bands as tangent. Further confirmation for the assignment of metallic conductivity for $LaTe_2$ stems from optical band gap determinations by measuring the fundamental absorption by diffuse reflection. Within the investigated frequency range of 10800–380 cm^{-1}, corresponding to an energy range of 1.33–0.05 eV, the reflectivity is typically metallic-like low and reveals no indications for a band gap.

DISCUSSION

In the past $LaTe_2$ was thought to be a metallic conductor because first principles calculations (7) assuming regular Te(1) square [4^4] nets revealed a Fermi surface which is mainly contributed from the Te(1) square sheets and has several large parallel branches that satisfy the nesting condition for a CDW transition. Our own investigations of magnetic susceptibility and fundamental absorption also suggest $LaTe_2$ to be metallic. The decisive differences of our results compared to former investigations are lying in the revised crystal structure parameters and the interpretation of these by first principles band structure calculations. To get a close correspondence to the distortion pattern of the homologous selenide, we have chosen a description of the crystal structure emphasizing the feature of the double-herringbone pattern, whereas in the compound $LaSe_2$ a simple-herringbone pattern is observed. According to Lee and Foran (9), the herringbone pattern is beyond the different investigated alternatives energetically the most favorable arrangement. The calculation of the electronic band structure including the computation of the COHP function has lead us to a quite different description emphasizing the secondary interactions between the dimers. In doing this we found two dimers linked together by a 90° interaction to

[1] $[2(\text{Te}) \times 4(s, p_x, p_y, p_z) \times 8(\text{formula units}) - 4(\text{unoccupied bands}) = 60] + 1(\text{La}(5d_{z^2-y^2})) = 61$.

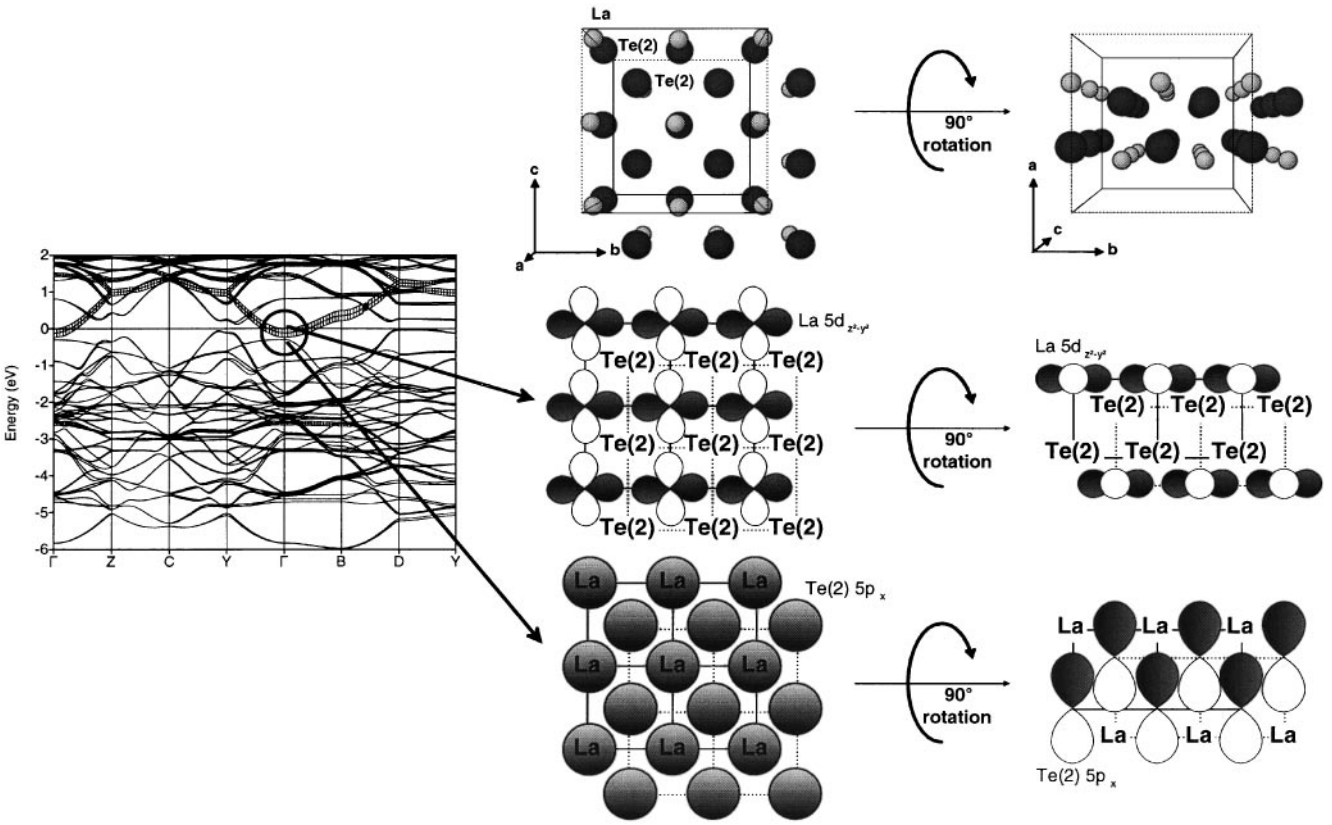

FIG. 10. Schematic representation of two selected crystal orbitals near E_F at the special point Γ for $LaTe_2$. For the purpose of orientation at the left side the band structure of $LaTe_2$ and at the top of the figure details of the crystal structure are given.

L-shaped [Te_4] units. But whatever description we choose, the metallic conductivity of an isolated square sheet is lost in the distorted CDW arrangement. Instead of this gap of ≈ 0.2 eV between bonding and antibonding Te(1) 5*p* states opens up at the Fermi level by the distortion and without further interactions $LaTe_2$ would be a small band gap semiconductor. Due to a direct La–La interaction at the special point Γ a single 5*d* band of La is lowered in energy to such a degree that this band is intersected by the Fermi energy. Because of the relative large interatomic La–La distances, this interaction is weak and results only in a small density of states at the Fermi level. Nevertheless, a certain

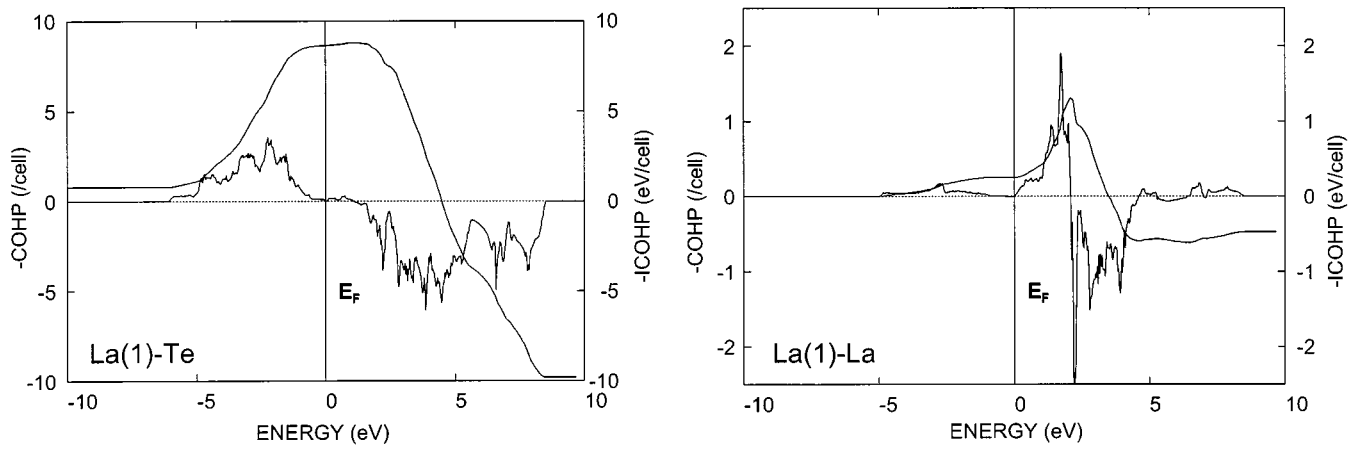

FIG. 11. Crystal orbital Hamiltonian population, COHP, exemplarily for the La(1)–Te and La(1)–La interactions in $LaTe_2$.

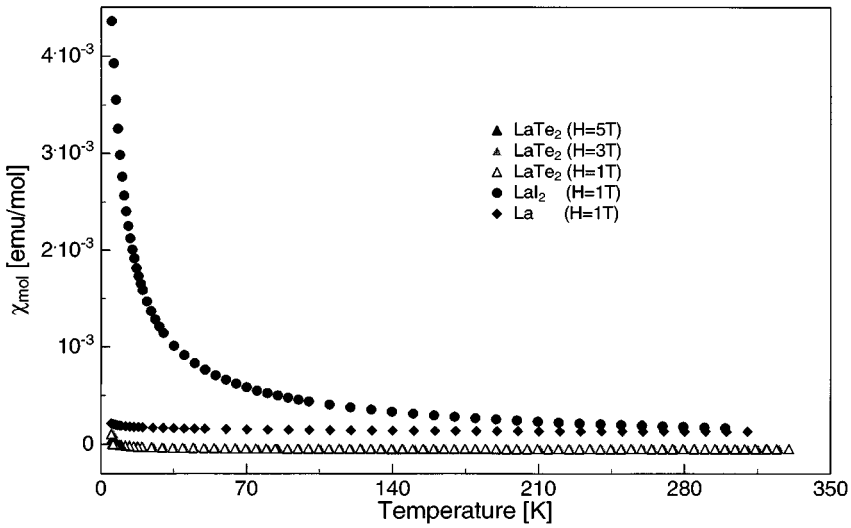

FIG. 12. Magnetic susceptibility of $LaTe_2$. For comparison the corresponding data of LaI_2 (27) with $\mu_B = 0.50$ B.M. and metallic La are also given.

density of states at the Fermi level is reached due to the contribution of Te(1) $5p_y$ and $5p_z$ bands. All in all a metallic conductivity characteristic is to be deduced for $LaTe_2$ in agreement with experimental data. This finding clearly demonstrates that a pure ionic formulation of $LaTe_2$ like $La^{3+}Te(1)^{-}Te(2)^{2-}$, as deduced after the inspection of the dispersion relation of an isolated distorted square sheet, is not adequate in this case. From the strong covalent La–Te interactions we have to conclude that the formal charge at La is significantly reduced, opening up the possibility of a direct La–La overlap. The Fermi surface of $LaTe_2$ is forming elliptically shaped electron pockets around special points Γ and reveals no indications for nesting. Referring to the results of the former electronic band structure calculations by Kikuchi (7) and Lee *et al.* (9) for the undistorted structural variant, the actual structure model of $LaTe_2$ can be regarded as a frozen CDW state with the surprising results that the metallic conductivity persists in the distorted material.

ACKNOWLEDGMENT

We gratefully acknowledge the Deutschen Forschungsgemeinschaft and the Fonds der Chemischen Industrie for financial support.

REFERENCES

1. A. A. Eliseev, V. G. Kuznestov, and E. I. Yarembash, *Zh. Strukt. Khim.* **5,** 640 (1964).
2. M.-P. Pardo, J. Flahaut, and L. Domange, *Bull. Soc. Chim. Fr.* 3267 (1964).
3. A. A. Eliseev, and V. G. Kuznetsov, *Neorg. Mater.* **1,** 692 (1965).
4. B. K. Norling, and H. Steinfink, *Inorg. Chem.* **5,** 1488 (1966).
5. K. A. Agaev, R. S. Gamidov, and Kh. S. Mamedov, *Issled. Obl. Neorg. Fiz. Khim.* 199 (1970).
6. Y. S. Kown, T. S. Park, K. R. Lee, J. M. Kim, Y. Haga, and T. Suzuki, *J. Magn. Magn. Mater.* **140–144,** 1173 (1995).
7. A. Kikuchi, *J. Phys. Soc. Jpn.* **67,** 1308 (1998).
8. P. S. Bénazeth, D. Carré, and P. Laruelle, *Acta Crystallogr. B* **38,** 33 (1982); P. S. Bénazeth, D. Carré, and P. Laruelle, *Acta Crystallogr. B* **38,** 37 (1982).
9. S. Lee and B. Foran, *J. Am. Chem. Soc.* **116,** 154 (1994).
10. E. DiMasi, B. Foran, M. C. Aronson, and S. Lee, *Phys. Rev. B* **54,** 13587 (1996).
11. G. M. Sheldrick, *SHELX*-97, *FORTRAN*77 *Program for the Determination and Refinement of Crystal Structures from Diffraction Data*, Göttingen, 1997; G. M. Sheldrick, *Acta Crystallogr. A* **46,** 467 (1990).
12. K. Stöwe, *Z. Anorg. Allg. Chem.* **622,** 1419 (1996).
13. P. W. Selwood, "Magnetochemistry," 2nd ed. Interscience Publishers, Inc., New York, 1956.
14. C. S. Pratt, B.A. Coyle, and J. A. Lbers, *J. Chem. Soc.* 2146 (1971).
15. G. B. Jameson, R. Schneider, E. Dubler, and H. R. Oswald, *Acta Crystallogr. B* **38,** 3016 (1982).
16. M. Grupe, and W. Urland, *J. Less-Common Met.* **170,** 271 (1991).
17. G. Krier, O. Jepsen, A. Burkhardt, and O.K. Andersen, *Tight binding LMTO-ASA Program Versions 4.7 and 4.7C,* Stuttgart, Germany.
18. O. Jepsen, and O. K. Andersen, *Z. Phys. B* **97,** 35 (1995).
19. F. Boucher, and R. Rousseau, *Inorg. Chem.* **37,** 2351 (1998).
20. M.-H. Whangbo, R. Hoffmann, and R. B. Woodward, *Proc. R. Soc. London, Ser. A* **366,** 23 (1979).
21. S. C. Miller, and W. F. Love, "Tables of Irreducible Representations of Space Groups and Co-Representation of Magnetic Space Groups." Pruett Press, Boulder, CO, 1967.
22. K. Stöwe, *J. Solid State Chem.* **149,** 123 (2000).
23. K. Stöwe, and F. R. Wagner, *J. Solid State Chem.* **138,** 160 (1998).
24. R. W. G. Wyckoff, "Crystal Structures," 2nd ed., Vol. 1. Interscience Publishers, New York, 1963.
25. E. Warkentin and H. Bärnighausen, " Third European Crystallography Meeting," Zürich, Switzerland, 1976.
26. J. H. Burrow, C. H. Maule, P. Strange, J. N. Tothill, and J. A. Wilson, *J. Phys. C: Solid State Phys.* **20,** 4115 (1987).
27. K. Stöwe, S. Tratzky, H. P. Beck, A. Jungmann, R. Claessen, R. Zimmermann, G. Meng, P. Steiner, and S. Hüfner, *J. Alloys Comp.* **246,** 101 (1997).